

NEW EVIDENCE FOR A SUBSTELLAR LUMINOSITY PROBLEM: DYNAMICAL MASS FOR THE BROWN DWARF BINARY GI 417BC*

TRENT J. DUPUY^{1,2}, MICHAEL C. LIU³, AND MICHAEL J. IRELAND^{4,5,6}

¹ The University of Texas at Austin, Department of Astronomy, 2515 Speedway C1400, Austin, TX 78712, USA

² Harvard-Smithsonian Center for Astrophysics, 60 Garden Street, Cambridge, MA 02138, USA

³ Institute for Astronomy, University of Hawai'i, 2680 Woodlawn Drive, Honolulu, HI 96822, USA

⁴ Department of Physics and Astronomy, Macquarie University, NSW 2109, Australia

⁵ Research School of Astronomy & Astrophysics, Australian National University, Canberra ACT 2611, Australia

⁶ Australian Astronomical Observatory, P.O. Box 296, Epping, NSW 1710, Australia

Received 2013 December 10; accepted 2014 June 2; published 2014 July 15

ABSTRACT

We present new evidence for a problem with cooling rates predicted by substellar evolutionary models that implies that model-derived masses in the literature for brown dwarfs and directly imaged planets may be too high. Based on our dynamical mass for GI 417BC (L4.5+L6) and a gyrochronology system age from its young, solar-type host star, commonly used models predict luminosities 0.2–0.4 dex lower than we observe. This corroborates a similar luminosity–age discrepancy identified in our previous work on the L4+L4 binary HD 130948BC, which coincidentally has nearly identical component masses ($\approx 50\text{--}55 M_{\text{Jup}}$) and age (≈ 800 Myr) as GI 417BC. Such a luminosity offset would cause systematic errors of 15%–25% in model-derived masses at this age. After comparing different models, including cloudless models that should not be appropriate for mid-L dwarfs like GI 417BC and HD 130948BC but actually match their luminosities better, we speculate the observed overluminosity could be caused by opacity holes (i.e., patchy clouds) in these objects. Moreover, from hybrid substellar evolutionary models that account for cloud disappearance, we infer the corresponding phase of overluminosity may extend from a few hundred million years up to a few gigayears and cause masses to be overestimated by up to 25%, even well after clouds disappear from view entirely. Thus, the range of ages and spectral types affected by this potential systematic shift in luminosity evolution would encompass most known directly imaged gas-giants and field brown dwarfs.

Key words: astrometry – binaries: close – brown dwarfs – infrared: stars – stars: fundamental parameters – stars: individual (GI 417, HD 130948)

Online-only material: color figures

1. INTRODUCTION

Models of substellar evolution have been notoriously under-constrained in the brown dwarf regime, but the last several years has seen significant progress. An increasing number of brown dwarf visual binaries have dynamical masses (Lane et al. 2001; Liu et al. 2008; Dupuy et al. 2009b, 2009c, 2010; Konopacky et al. 2010), and there are now several transiting brown dwarfs that provide tests of the mass–radius relationship (e.g., Stassun et al. 2006; Deleuil et al. 2008; Anderson et al. 2011; Johnson et al. 2011; Siverd et al. 2012). However, the total energy output of substellar objects as a function of mass and age has still barely been tested, despite the fact that these fundamental predictions underpin the mass estimates for all brown dwarfs and extrasolar planets that lack directly determined masses.

Until now there has been only been one system that enables a robust test of substellar luminosity evolution because of the demanding requirements of both precise mass, age, and luminosity determinations.⁷ In Dupuy et al. (2009b), we found that the

components of the brown dwarf visual binary HD 130948BC were $\approx 2\times$ more luminous than expected from models given their age and mass. This was a surprising result, given that the bulk properties of brown dwarfs from evolutionary models were thought to be relatively robust against the boundary conditions of models by several hundred million years. Furthermore, there has been no satisfactory theoretical explanation of how such a luminosity problem might arise; for example, even custom magnetic models of HD 130948BC cannot match the observations (Mullan & MacDonald 2010). We also note that an earlier dynamical mass measurement for the substellar companion GI 802B hinted at a similar luminosity problem due to its likely thick disk membership being inconsistent with an age of ~ 2 Gyr inferred from evolutionary models using its mass and near-infrared flux (Ireland et al. 2008). Another hint came from HR 7672B, which Crepp et al. (2012) found to be a factor of ~ 2 ($\sim 1.2\sigma$) overluminous given its mass and gyrochronology age. With no other systems to test models, it has not yet been clear if there truly is a problem in predictions of substellar luminosity evolution, which could affect model-derived mass estimates and thereby have wide-ranging implications, or if our one test case was simply an unfortunate outlier.

We present a dynamical mass for the L dwarf binary GI 417BC that provides new evidence for the same substellar luminosity problem found for HD 130948BC. Kirkpatrick et al. (2000)

* Data presented herein were obtained at the W. M. Keck Observatory, which is operated as a scientific partnership among the California Institute of Technology, the University of California, and the National Aeronautics and Space Administration. The Observatory was made possible by the generous financial support of the W. M. Keck Foundation.

⁷ In principle, the giant planets of the solar system also allow tests of substellar luminosity evolution but with very different assumptions for internal composition and structure such as the possible presence of metal-rich cores. In the latest models of Fortney et al. (2011), Jupiter is only slightly (0.04 dex) under-luminous compared to models, while Saturn is 0.20 dex over-luminous. Special mechanisms have been proposed to explain Saturn's excess luminosity

such as helium rain (e.g., Stevenson 1980) or, more recently, layered convection driven by a steep molecular weight gradient (Leconte & Chabrier 2013).

originally identified the Gl 417BC system (unresolved) as the lithium-bearing L4.5 dwarf 2MASSW J1112257+354813. Kirkpatrick et al. (2001) subsequently found that it was co-moving at a distance of 90'' from the star Gl 417, now dubbed Gl 417A.⁸ The revised *Hipparcos* parallax for Gl 417A is 45.61 ± 0.44 mas (van Leeuwen 2007), giving a distance of 21.93 ± 0.21 pc to the system and projected separation of 1970 ± 20 AU for the Gl 417AB pair. Kirkpatrick et al. (2001) used age indicators for the primary star such as chromospheric activity, rotation, and lithium absorption to estimate an age of 80–300 Myr for the system. This age range implied a substellar mass for 2MASSW J1112257+354813, corroborated by the detection of lithium in its spectrum. Bouy et al. (2003) presented *Hubble Space Telescope*/Wide-Field Planetary Camera 2 (*HST*/WFPC2) images resolving this object as a binary, named Gl 417BC, with a projected separation of 70 mas (or 1.5 AU) and an estimated orbital period of <10 yr. This made Gl 417BC one of the most likely substellar binaries to yield a dynamical mass from determining the visual orbit of the brown dwarfs around each other. However, unlike some substellar companions, Gl 417BC is too distant from its host star to use natural guide star adaptive optics (AO), and there has been no resolved astrometry of Gl 417BC published in more than a decade since it was discovered to be a binary.

We have obtained Keck laser guide star (LGS) AO imaging of Gl 417BC. Combined with the original *HST* imaging, our astrometric data set spans more than 13 yr and enables us to determine a precise total dynamical mass for this binary. Moreover, Gl 417A provides a much more precise age estimate than is typically possible for stars in the field population because of its youth. Therefore, Gl 417BC now joins HD 130948BC as the only brown dwarf binaries with precisely determined masses and ages.

2. ASTROMETRIC MONITORING OF Gl 417BC

2.1. Keck/NIRC2 LGS AO

We used the facility near-infrared camera NIRC2 with the LGS AO system at the Keck II telescope (Wizinowich et al. 2006; van Dam et al. 2006) to image the binary Gl 417BC at eight epochs spanning 2007 March 25 UT to 2014 May 9 UT. We obtained data in standard Mauna Kea Observatories (MKO) photometric bandpasses (Simons & Tokunaga 2002; Tokunaga et al. 2002).⁹ The LGS was kept centered in NIRC2's narrow camera field-of-view while we obtained dithered images of the target. The wavefront sensor recorded flux from the LGS equivalent to a $V \approx 9.5$ – 10.4 mag star. For tip-tilt correction we used the star SDSS J111229.47+354813.2, which is 46'' away from Gl 417BC, and the lower bandwidth sensor monitoring this source recorded flux equivalent to a $R \approx 17.5$ – 18.0 mag star. We note that this tip-tilt star was not provided by the standard Keck IDL routine FINDTTREF—the tool used by most Keck LGS observers to determine if a target has suitable reference stars—because it does not exist in the USNO-B catalog (Monet et al. 2003). However, we noticed it by eye in the *HST*/WFPC2 data and in Digital Sky Survey images, and it also appears in subsequently released Sloan Digital Sky Survey (SDSS) data.

Our procedure for reducing and analyzing Keck LGS data is described in detail in our previous work (Dupuy et al.

2009b, 2009c, 2010). To summarize briefly, we measure binary parameters using the StarFinder software package (Diolaiti et al. 2000) when the separation is large and by fitting three-component Gaussians when the components are too close for StarFinder to robustly identify two distinct sources. We derive uncertainties by applying our fitting method to artificial binary images constructed from images of point-spread function (PSF) reference stars with similar FWHM and Strehl ratio, as well as by checking the scatter between individual dithered images. We use the NIRC2 astrometric calibration from Yelda et al. (2010), which includes a correction for the nonlinear distortion of the camera and has a pixel scale of 9.952 ± 0.002 mas pixel⁻¹ and an orientation for the detector's +y-axis of $+0^\circ.252 \pm 0^\circ.009$ east of north. Figure 1 shows contour plots of our imaging data at each epoch, stacked for the purposes of display.

In Table 1, we present the results of our Keck imaging, including the FWHM and Strehl ratio at each epoch along with the derived binary parameters. As a check on these parameters, we note that the K_S -band flux ratio is consistent between the five epochs for which we have data in that bandpass with a χ^2 of 4.8 for 4 degrees of freedom (dof; $p = 0.31$). The weighted average and corresponding error is $\Delta K_S = 0.413 \pm 0.020$ mag.

2.2. HST/WFPC2

The *HST*/WFPC2 discovery images of Gl 417BC were taken on 2001 February 14 UT as part of GO-8581 (PI Reid), with one image each in F814W and F1042M. We used the F814W image for measuring astrometry, because the PSF is smaller at shorter wavelengths and thus enables more robust deblending of this tight 1.6-pixel binary. As in our previous work (e.g., Liu et al. 2008; Dupuy et al. 2009a), we applied a binary fitting routine based on the TinyTim model of the *HST* PSF (Krist 1995) to both the data and numerous simulated binary images constructed from single stars observed by *HST*/WFPC2. The simulated binaries were constrained to be within 0.2 pixels of the actual configuration of Gl 417BC, and the difference between the input and output values were used to determine the rms scatter and systematic offsets in the binary parameters. We found the offsets to be somewhat less than the scatter in separation (-1.9 ± 2.3 mas), position angle (P.A.; $+0^\circ.6 \pm 1^\circ.5$), and flux ratio ($+0.04 \pm 0.07$ mag), where our quoted values are offset \pm rms.

Table 1 shows the derived binary parameters after applying the offsets from our simulations and using the rms values for the errors. Our results are somewhat inconsistent with the parameters reported in Bouy et al. (2003) by 6.1 mas (1.7σ), $3^\circ.4$ (1.6σ), and 0.52 mag (4.0σ). However, we note that their paper adopted a simplification in determining errors, namely that a single value for the uncertainty in given parameter was used for all 60–150 mas (1.3–3.3 pixel) binaries. This obscures the fact that the tighter binaries over this range should have larger uncertainties than the wider ones. For example, their Figures 2 and 3 illustrate this well, and their larger truth-minus-fitted scatter over the narrower 60–70 mas separation range is sufficient to explain the apparent discrepancies between our two sets of binary parameters. There is much larger scatter in P.A. and flux ratio than is accounted for by their single uncertainty values for these parameters, and there is an apparent trend for these tightest binaries that their fitting overestimates the separation by ≈ 2 – 3 mas. In the following, we will conservatively consider both our own *HST*/WFPC2 astrometry that relies on simulations tailored specifically to Gl 417BC as well as the values reported by Bouy et al. (2003).

⁸ Some other names for Gl 417A are HD 97334, BD+36 2162, MN UMa, HR 4345, and HIP 54745.

⁹ See the Appendix of Liu et al. (2012) for a discussion of the *Y* bandpass of NIRC2 compared to other photometric systems.

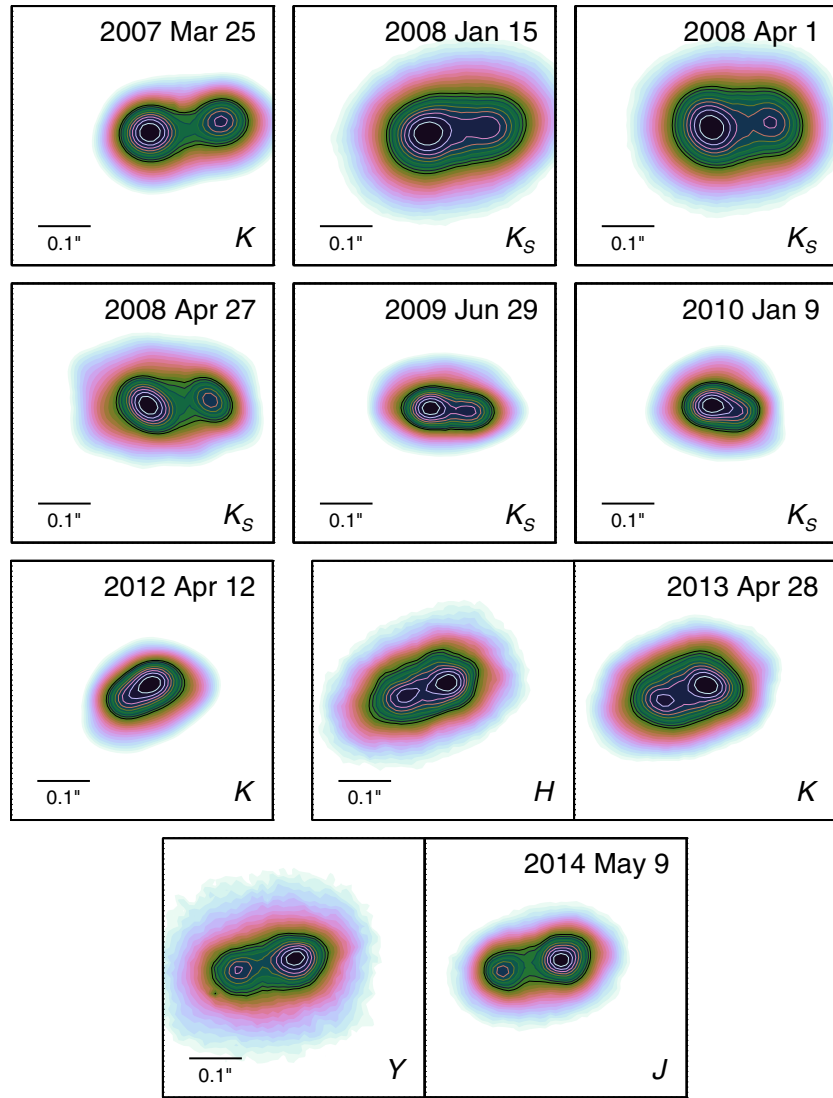


Figure 1. Contour plots of our Keck LGS AO images from which we derive astrometry and flux ratios (Table 1). Contours are in logarithmic intervals from unity to 7% of the peak flux in each band. The image cutouts are all the same size and have the same native pixel scale, and we have rotated them such that north is up for display purposes.

(A color version of this figure is available in the online journal.)

Table 1
Relative Astrometry and Photometry for GI 417BC

Date (UT)	Airmass	Filter	FWHM (mas)	Strehl Ratio	ρ (mas)	P.A. ($^\circ$)	Δm (mag)
2001 Feb 14	...	F814W	63.9 ± 2.3	76.2 ± 1.5	0.55 ± 0.07
2007 Mar 25 ^a	1.301	<i>K</i>	91 ± 5	0.15 ± 0.02	140.4 ± 0.9	278.84 ± 0.28	0.347 ± 0.025
2008 Jan 15	1.112	<i>K_S</i>	115 ± 6	0.074 ± 0.007	128.6 ± 1.2	276.3 ± 0.8	0.35 ± 0.04
2008 Apr 1	1.331	<i>K_S</i>	112 ± 4	0.078 ± 0.011	125.2 ± 0.8	275.3 ± 1.0	0.41 ± 0.03
2008 Apr 27	1.422	<i>K_S</i>	85 ± 4	0.12 ± 0.02	124.7 ± 0.6	274.2 ± 0.6	0.47 ± 0.04
2009 Jun 29	1.512	<i>K_S</i>	68 ± 2	0.21 ± 0.03	83.8 ± 1.5	266.1 ± 1.4	0.47 ± 0.11
2010 Jan 9	1.072	<i>K_S</i>	66 ± 3	0.23 ± 0.04	63.3 ± 1.3	258.0 ± 1.8	0.43 ± 0.08
2012 Apr 12	1.067	<i>K</i>	73 ± 5	0.20 ± 0.03	65.3 ± 1.8	123.4 ± 2.8	0.34 ± 0.14
2013 Apr 28	1.157	<i>H</i>	78 ± 6	0.051 ± 0.004	100.8 ± 0.5	108.4 ± 1.9	0.26 ± 0.09
	1.136	<i>K</i>	87 ± 10	0.111 ± 0.017	101.0 ± 1.4	110.0 ± 2.2	0.28 ± 0.13
2014 May 9	1.107	<i>Y_{NIRC2}</i>	78 ± 10	0.018 ± 0.004	115.8 ± 0.6	102.0 ± 0.3	0.40 ± 0.04
	1.097	<i>J</i>	69 ± 8	0.047 ± 0.011	116.8 ± 0.8	101.2 ± 0.4	0.44 ± 0.04

Notes. The first epoch of data is from *HST*/WFPC2-PC, and the other epochs are our new Keck LGS AO measurements. For the Keck images, Strehl ratios and FWHM were computed using the publicly available routine NIRC2STREHL.

^a This epoch was first reported in Dupuy & Liu (2012).

Table 2
Derived Orbital Parameters for GI 417BC

Parameter	Best Fit	Median	68.3% c.l.	95.4% c.l.
Orbital period P (yr)	15.65	15.65	15.56, 15.73	15.49, 15.81
Semimajor axis a (mas)	130.1	130.0	129.6, 130.5	129.2, 130.9
Eccentricity e	0.106	0.105	0.102, 0.109	0.099, 0.112
Inclination i ($^\circ$)	102.9	102.9	102.4, 103.4	101.9, 103.9
P.A. of the ascending node Ω ($^\circ$)	101.03	101.01	100.79, 101.23	100.57, 101.46
Argument of periastron ω ($^\circ$)	348	347	343, 352	339, 356
Time of periastron $T_0 - 2456664.5$ (JD)	0	-10	-70, 50	-130, 110
Total mass (M_\odot): fitted	0.0949	0.0947	0.0934, 0.0959	0.0923, 0.0972
Total mass (M_\odot): final	0.0949	0.0947	0.0916, 0.0976	0.0888, 0.1008

Notes. For each parameter we report the value corresponding to the best fit (i.e., the lowest χ^2 in the MCMC chain, $\chi_{\min}^2 = 21.56$) along with the median of the posterior distribution and the shortest intervals containing 68.3% and 95.4% of the chain steps (i.e., 1σ and 2σ confidence limits). For clarity, the time of periastron passage is reported relative to the best-fit value of 2456664.5 JD (i.e., 2014 January 7 00:00 UT). Without resolved radial velocities, there is a 180° ambiguity in both Ω and ω . The “fitted” total mass represents the results from fitting the observed orbital motion without accounting for the parallax error. The “final” total mass includes the additional error in the mass due to the error in the parallax.

3. ORBITAL PARAMETERS OF GI 417BC

The relative astrometry for GI 417BC presented in Table 1 spans more than 13 yr in time and 334° in P.A., enabling us to robustly determine its orbital parameters for the first time. As in our previous work (e.g., Liu et al. 2008; Dupuy et al. 2009b), we use a Markov Chain Monte Carlo (MCMC) technique to determine the posterior distributions of all quantities. We briefly summarize our procedure, as we have made some minor modifications to our code compared to our previous work. As before, we use a Metropolis–Hastings jump acceptance criterion with Gibbs sampling that alters only one parameter at each step in the chain (e.g., see Ford 2005). Before running our science chains, we first run a test chain according to the method outlined by Ford (2006) in order to determine optimal step sizes for each parameter (see Section 2.4 of Dupuy & Liu 2012 for more details). We then run 20 science chains starting at different points in parameter space, chosen by adding Gaussian noise scaled by the step sizes to the best-fit values. We find the best-fit values in advance by using our least-squares minimization routine based on the MPFIT IDL package (Markwardt 2009), as described in Dupuy et al. (2010).

Each of our 20 Markov chains has 10^7 steps, with every hundredth step saved. We chose to step in parameters that would result in appropriate uninformative (i.e., flat) prior assumptions. For the orbital period (P) and semimajor axis (a), our prior is log-flat as we stepped in $\log P$ and $\log a$. The priors in eccentricity (e), argument of periastron (ω), time of periastron passage (T_0), and P.A. of the ascending node (Ω) are linear-flat as we stepped in $\sqrt{e} \cos \omega$, $\sqrt{e} \sin \omega$, T_0 , and Ω . Finally, our inclination (i) prior assumes randomly distributed viewing configurations by stepping in $\cos i$. In our previous work we modified the parameters being stepped along after every 5×10^5 iterations in order to increase the efficiency of exploring of a “curved” region of low χ^2 in parameter space. However, for well-determined orbits like the case of GI 417BC this is not necessary and the increased computational time needed for such optimization ultimately results in lowered efficiency.

Table 2 shows the resulting orbital parameters found by our MCMC analysis, and Figure 2 shows our relative astrometry alongside the best-fit orbit. The lowest χ^2 value in our chains is 21.56 (17 dof), which has a probability of 0.202 according to the χ^2 distribution, implying that our adopted astrometric errors are reasonable. The parameter values at this chain step are considered the best-fit orbit, which is identical to that found

by our MPFIT routine. In Table 2, we give these best-fit values along with the median and 1σ and 2σ confidence intervals for each parameter chain. We define our confidence intervals as the smallest range of values that captures 68.3% and 95.4% of the distribution. We adopt this approach in order to report the most likely range of parameter values from distributions that are often asymmetrical, sometimes sharply bounded (e.g., $0 \leq e < 1$), and in principle could be multi-modal. In such cases, intervals computed from the 68.3% and 95.4% of chain steps centered on the median (like we have reported in previous work) may not capture the peak of the posterior distribution. We note that the confidence intervals we report here all include the best-fit parameter values. We used the ensemble of chains to compute Gelman–Rubin statistics for all parameters and check for convergence and found Gelman–Rubin values of $\lesssim 1.001$. These imply that all parameters are converged given the standard criterion requiring Gelman–Rubin values < 1.2 (Ford 2005).

Combining our orbit with the parallax distance allows us to measure the total mass (M_{tot}) of GI 417BC directly from Kepler’s third law. We find $M_{\text{tot}} = 0.095 \pm 0.003 M_\odot$ (3.2% error), with 1.3% of the error coming from the uncertainty in the orbital parameters and 2.9% from the parallax uncertainty. We investigated the impact of using the different *HST*/WFPC2 astrometry discussed in Section 2.2 by computing additional MCMC chains. When we used the separation and P.A. as reported by Bouy et al. (2003) for the discovery epoch, all resulting orbital parameter distributions agreed well, with the 1σ confidence intervals overlapping in all cases and a minimum χ^2 value nearly identical to ours. For a direct comparison of the total mass implied by the different sets of astrometry, we ignore the parallax error and find that the 1σ mass interval using the Bouy et al. (2003) astrometry overlaps with our 1σ range of 0.0934–0.0959 M_\odot . Thus, the choice of *HST*/WFPC2 astrometry does not have a significant impact on the resulting dynamical mass, likely because the orbit fit is dominated by our more precise and more numerous Keck LGS AO astrometric data.

4. THE AGE AND COMPOSITION OF THE GI 417 SYSTEM

The age and composition of all three components in the GI 417 system can be established from the solar-type primary star GI 417A under the conservative assumption that the system formed coevally from the same bulk material. Valenti & Fischer

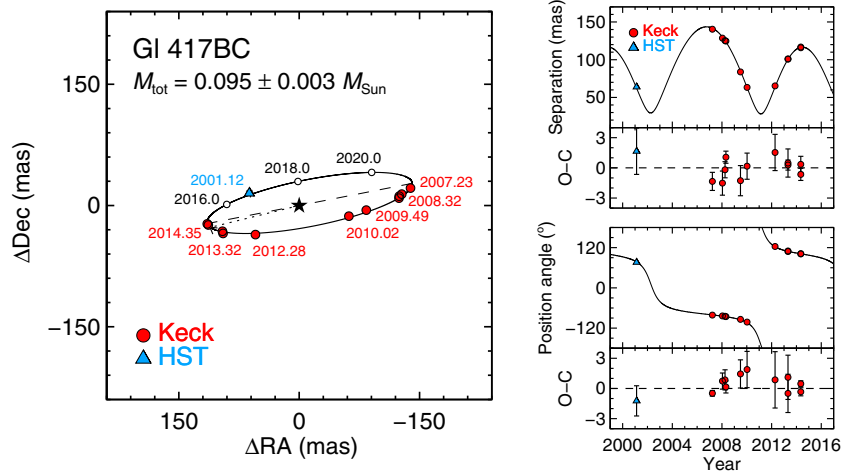


Figure 2. Left: relative astrometry for Gl 417BC along with our best-fit orbit. Error bars for the data are smaller than the plotting symbols. The short dotted line indicates the time of periastron passage, the long dashed line shows the line of nodes, and small empty circles show predicted future locations. Right: measurements of the projected separation and P.A. of Gl 417BC. The best-fit orbit is shown as a solid line. The bottom panels show the observed minus computed ($O - C$) measurements with observational error bars.

(A color version of this figure is available in the online journal.)

(2005) report a slightly super-solar metallicity of $[\text{Fe}/\text{H}] = 0.09 \pm 0.03$ dex. In the following analysis, due to a lack of substellar evolutionary and atmospheric models that sample metallicity at such a fine level, we will compare to solar metallicity models but also consider the impact of this limitation on our resulting interpretations.

Numerous methods for estimating the age of a solar-type star such as Gl 417A are available. Foremost among these in terms of claimed precision is gyrochronology, which relies on the fact that stars lose angular momentum with age in a predictable way (e.g., Skumanich 1972). Recent advances in obtaining rotation periods and membership data for large samples of stars in clusters has enabled a calibration of this spin-down against cluster isochronal ages, one of the most trusted clocks in astrophysics. Barnes (2007) defined an empirical formalism to account for the fact that the rate of change in stellar rotation period depends on mass, which he parameterized as a function of $(B - V)_0$ color. We have used these relations with the improved calibration from Mamajek & Hillenbrand (2008) to derive the age of Gl 417A. For the rotation period, we use the five independent measurements obtained by Gaidos et al. (2000) over six years. The weighted average and rms of these rotation periods is 8.27 ± 0.17 days, which agrees well with the period of 8 days reported by Baliunas et al. (1996). Combined with the $B - V$ color of Gl 417A (0.600 ± 0.010 mag, neglecting reddening; Mermilliod & Mermilliod 1994), the gyrochronology relation yields an age of $\log(t/\text{yr}) = 8.87 \pm 0.08$ dex (750^{+150}_{-120} Myr), where we have computed errors in a Monte Carlo fashion as described in Section 4.3 of Dupuy et al. (2009b).

Perhaps the next best calibrated empirical relations for determining age are those that track magnetic activity either using Ca II H and K chromospheric emission or X-ray emission. Using data from Mount Wilson that spans approximately 20 yr, Baliunas et al. (1996) report a time-averaged value of $\log R'_{\text{HK}} = -4.422$ dex for Gl 417A. This value is in good agreement with the single-epoch value of $\log R'_{\text{HK}} = -4.368$ dex reported by Gray et al. (2003), as well as the older Mount Wilson value of $\log R'_{\text{HK}} = -4.40$ dex from Soderblom (1985). We use the Baliunas et al. (1996) $\log R'_{\text{HK}}$ value to compute an age for Gl 417A from the chromospheric activity relations derived

by Mamajek & Hillenbrand (2008). We use the method recommended by these authors which first converts the $\log R'_{\text{HK}}$ value to a Rossby number (i.e., rotation period divided by the convective turnover timescale τ_{conv}), which we find to be 0.52 ± 0.10 , adopting an uncertainty of 0.10 as suggested by Mamajek & Hillenbrand (2008) when using high quality Mount Wilson data. The Rossby number is then converted to a rotation period by estimating τ_{conv} from the star's color, and this step yields $\tau_{\text{conv}} = 9.1$ days and thus an activity-derived rotation period of 4.7 ± 0.9 days. This is finally converted to an age via their gyrochronology relation, which gives $\log(t/\text{yr}) = 8.44 \pm 0.18$ dex. This is strikingly different from the age derived directly from the actual rotation period (2.2σ , given the adopted uncertainties). We note that if we use Equation 3 from Mamajek & Hillenbrand (2008), which gives a simpler relation just between $\log R'_{\text{HK}}$ and age, we find a consistent but less precise age ($\log(t/\text{yr}) = 8.55 \pm 0.25$ dex) that is still 1.2σ younger than the gyrochronology age.

Mamajek & Hillenbrand (2008) provide a similar method for estimating age from X-ray emission. For Gl 417A, Hempelmann et al. (1995) found an X-ray to bolometric luminosity ratio of $\log R_X \equiv \log(L_X/L_{\text{bol}}) = -4.60 \pm 0.06$ dex. Using the method proposed by Mamajek & Hillenbrand (2008), we derive a Rossby number of 0.68 ± 0.25 from this $\log R_X$ value, and thus an activity-derived rotation period of 6.2 ± 4.9 days. This agrees well with the actual measured rotation period and thus results in an age of $\log(t/\text{yr}) = 8.72 \pm 0.67$ dex that is consistent with the gyrochronology age.

Other indicators provide some information about the age of Gl 417A, though not at the same precision as rotation and activity. Duncan (1981) measured a lithium abundance of $\log N_{\text{Li}} = 2.38$ dex ($W_{\text{Li}} = 0.081 \text{ \AA}$) for Gl 417A. Thus, given its effective temperature ($T_{\text{eff}} = 5898 \text{ K}$; Valenti & Fischer 2005), Gl 417A lies somewhat below (i.e., older than) the mean relations of $\log N_{\text{Li}}$ versus T_{eff} for members of the 625-Myr-old Praesepe and Hyades clusters and significantly below the 125-Myr-old Pleiades cluster (Soderblom et al. 1993a, 1993b). A comparison of Gl 417A's fundamental properties to stellar evolution models could offer an isochronal age, but as is the case for many field stars the analysis of Takeda et al. (2007) gives only an upper limit for the age of Gl 417A (< 2.9 Gyr,

68.3% confidence). Finally, we compute the heliocentric space motion of Gl 417A, $(U, V, W) = (-15.99 \pm 0.17, -23.31 \pm 0.23, -11.40 \pm 0.12)$ km s⁻¹, with U positive toward the galactic center, based on the new *Hipparcos* parallax and proper motion from van Leeuwen (2007) and a radial velocity of -3.68 ± 0.10 km s⁻¹ compiled by de Bruijne & Eilers (2012). The space motion of Gl 417A has not linked it to any known moving groups or associations (e.g., Gaidos et al. 2000), and we also find no such linkages using the online calculators of Malo et al. (2013) and Gagné et al. (2014).

We briefly note that Gl 417BC itself could provide a system age constraint from spectroscopic signatures of low surface gravity. Kirkpatrick et al. (2008) discussed this system in detail, and without resolved optical spectroscopy they made the reasonable assumption that the integrated-light spectrum was dominated by Gl 417B ($\Delta F_{814W} = 0.55 \pm 0.07$ mag). They found that Gl 417B is practically indistinguishable from normal, older field L4–L5 dwarfs. The alkali lines that typically weaken for low gravity objects appear normal, with the possible exception of Rb I (7800 Å, 7948 Å). They also note the TiO bandhead at 8200 Å might be weaker than normal, though we note this could also be due to dilution from the later type secondary component. Kirkpatrick et al. (2008) conclude that Gl 417B is only “slightly peculiar” because the spectroscopic signatures are not as obvious as in lower surface gravity objects. Allers & Liu (2013) examined the near-infrared integrated-light spectrum of Gl 417BC and assigned a field gravity classification (FLD-G) because multiple gravity-sensitive features were consistent with normal field objects. Overall, we find that the spectrum of Gl 417BC agrees with our older gyrochronology age of 750^{+150}_{-120} Myr and is somewhat inconsistent with the originally published age estimate of 80–300 Myr from Kirkpatrick et al. (2001).

In summary, the most robust age available for the Gl 417 system is from gyrochronology of the solar-type primary, $\log(t/\text{yr}) = 8.87 \pm 0.08$ dex, which implies that Gl 417A is somewhat older or consistent with the Hyades. Only one age dating method is apparently inconsistent with this. The chromospheric emission of Gl 417A traced by Ca II H and K seems to imply a much younger age of $\log(t/\text{yr}) = 8.32 \pm 0.21$ dex according to the calibration of Mamajek & Hillenbrand (2008). However, examining the range of activity levels for members of young clusters reveals that Gl 417A, with $\log R'_{\text{HK}} = -4.422$ dex, is actually comfortably within the 68% confidence intervals of both the 500-Myr-old Ursa Majoris group ($\log R'_{\text{HK}} = -4.39$ dex to -4.57 dex) and the 625-Myr-old Hyades cluster ($\log R'_{\text{HK}} = -4.38$ dex to -4.56 dex). Thus, the chromospheric activity traced by Ca II H and K is not actually inconsistent with all the other indicators, including activity traced by X-ray emission, that agree with the gyrochronology age of 750^{+150}_{-120} Myr. This agrees with chromospheric and X-ray activity being manifestations of a magnetic dynamo that is driven by rotation, which is also likely why rotation–age relations show less scatter than activity–age relations.

5. SPECTRAL TYPES AND BOLOMETRIC LUMINOSITIES

Dupuy & Liu (2012) report resolved spectral types for the components of Gl 417BC from spectral decomposition using its integrated-light infrared spectrum along with the measured K -band flux ratio (the March 2007 data in our Table 1 are the same as in their Table 5). Dupuy & Liu (2012) found infrared types of $L4.5 \pm 1$ and $L6 \pm 1$ for the primary and

secondary components, respectively, in good agreement with the integrated-light optical spectral type of L4.5 reported by Kirkpatrick et al. (2000). Our new data presented here would not significantly better constrain the resolved spectral types and are in good agreement with the Dupuy & Liu (2012) estimates of flux ratios in other bandpasses ($\Delta J = 0.26 \pm 0.34$ mag, $\Delta H = 0.32 \pm 0.15$ mag), so we simply adopt the Dupuy & Liu (2012) spectral types here.

To derive bolometric luminosities (L_{bol}) for both components, we used our resolved K -band photometry and the bolometric correction–spectral type relation from Liu et al. (2010). We converted the integrated-light photometry of Gl 417BC from 2MASS (Cutri et al. 2003) to the MKO system using synthetic photometry derived from the SpeX prism spectrum of Gl 417BC itself (Burgasser et al. 2010). The resulting K -band photometry is 13.29 ± 0.03 mag and 13.63 ± 0.03 mag for Gl 417B and Gl 417C, respectively. When calculating bolometric corrections we account for both the uncertainties in the resolved spectral types and scatter in the polynomial relations of Liu et al. (2010), the latter of which dominates, and we find $BC_K = 3.31 \pm 0.08$ mag for Gl 417B and $BC_K = 3.27 \pm 0.09$ mag for Gl 417C. Therefore, we arrive at $\log(L_{\text{bol}}/L_{\odot})$ values of -4.06 ± 0.04 dex and -4.18 ± 0.04 dex for the two components, respectively, where the uncertainty in the distance is negligible compared to the uncertainties in bolometric corrections. This corresponds to an integrated-light bolometric flux of $L_{\text{bol}} = (1.54 \pm 0.10) \times 10^{-4} L_{\odot}$. As a check, we computed the flux over the wavelength range of 0.80–2.55 μm from the integrated-light SpeX spectrum of the binary and found $L_{\text{NIR}} = (0.84 \pm 0.02) \times 10^{-4} L_{\odot}$, which is $55\% \pm 4\%$ of our total estimated L_{bol} . In comparison, for a BT-Settl model (Allard et al. 2011) with properties similar to the components of Gl 417BC that we derive in Section 6, $T_{\text{eff}} = 1700$ K and $\log(g) = 5.0$ dex (cgs), 54% of the bolometric flux emerges over 0.80–2.55 μm . Thus, our estimated L_{bol} values are in good agreement with direct integration of the near-IR spectral energy distribution.

A summary of all the measured quantities for Gl 417BC quoted above are summarized in Table 3. In the following analysis, we track the covariance in luminosity ratio with other parameters like mass ratio and the temperature difference between the two binary components, all of which depend commonly on the uncertainties in distance and bolometric correction. For consistency, we also recalculate the bolometric luminosities of the components of HD 130948BC in the same fashion as Gl 417BC described above. Using the photometry and spectral types from Dupuy et al. (2009b) we find $\log(L_{\text{bol}}/L_{\odot})$ values of -3.81 ± 0.03 dex and -3.89 ± 0.03 dex for HD 130948B and HD 130948C, respectively, only 0.01 dex different from our previously published values but with smaller errors thanks to the improved bolometric correction relation from Liu et al. (2010).

6. MODEL-DERIVED PROPERTIES FOR Gl 417BC

Stellar evolutionary models predict how the properties of brown dwarfs depend on age for a given mass and composition. Thus with a directly measured total mass for Gl 417BC and an age and composition inferred from the primary star Gl 417A, we can derive model-predicted values for L_{bol} , T_{eff} , etc. Conversely, we can use a directly measured property like L_{bol} along with the system mass to infer the age from evolutionary models, or use L_{bol} and age to infer mass. These mirrored scenarios correspond respectively to “mass benchmarks” and “age benchmarks,” objects for which at least two of three fundamental properties are

Table 3
Measured Properties of Gl 417BC

Property	Gl 417B	Gl 417C	Ref.
M_{tot} (M_{Jup})	99 ± 3		1, 2
$\log(t/\text{yr})$	8.87 ± 0.08		1
Semimajor axis (AU)	2.85 ± 0.03		1, 2
d (pc)	21.93 ± 0.21		2
Spectral type	$L4.5 \pm 1.0$	$L6.0 \pm 1.0$	3
Y (mag)	16.37 ± 0.06	16.77 ± 0.06	1, 4
J (mag)	15.05 ± 0.04	15.49 ± 0.04	1, 4
H (mag)	14.19 ± 0.05	14.45 ± 0.06	1, 4
K (mag)	13.29 ± 0.03	13.63 ± 0.03	1, 4
$Y - J$ (mag)	1.32 ± 0.06	1.28 ± 0.07	1, 4
$J - H$ (mag)	0.86 ± 0.06	1.04 ± 0.07	1, 4
$H - K$ (mag)	0.91 ± 0.06	0.82 ± 0.07	1, 4
$J - K$ (mag)	1.76 ± 0.05	1.86 ± 0.05	1, 4
M_Y (mag)	14.67 ± 0.07	15.07 ± 0.07	1, 2, 4
M_J (mag)	13.34 ± 0.04	13.78 ± 0.05	1, 2, 4
M_H (mag)	12.49 ± 0.06	12.74 ± 0.06	1, 2, 4
M_K (mag)	11.58 ± 0.04	11.93 ± 0.04	1, 2, 4
BC_K (mag)	3.31 ± 0.08	3.27 ± 0.09	1, 5
$\log(L_{\text{bol}}/L_{\odot})$	-4.06 ± 0.04	-4.18 ± 0.04	1
$\Delta \log(L_{\text{bol}})$	0.12 ± 0.05		1

Notes. All near-infrared photometry on the MKO system, with Y -band specifically on the UKIRT system assuming that our Keck flux ratio $\Delta Y_{\text{NIRC2}} = \Delta Y_{\text{MKO}}$ due to the similar component spectral types.

References. (1) This work; (2) van Leeuwen (2007); (3) Dupuy & Liu (2012); (4) Cutri et al. (2003); (5) Liu et al. (2010).

measured, as discussed in detail by Liu et al. (2008). In fact, since mass and luminosity can typically both be measured to high precision (3%–10%), they are the preferred pair of parameters with which to infer other properties from models, even if age (typical precision $\gtrsim 25\%$) and mass are both available.

We consider multiple substellar evolutionary calculations in our analysis. The Lyon Dusty models (Chabrier et al. 2000) are among the most commonly used, and they should be appropriate for the components of Gl 417BC because their mid-L spectral types imply cloud opacity above the photosphere. Saumon & Marley (2008, hereinafter SM08) were the first to compute evolutionary models in which cloud opacity changes with time. Their hybrid models assume the photosphere smoothly transitions from cloudy to cloudless as objects cool from effective temperatures of 1400 K–1200 K. The components of Gl 417BC turn out to both be warmer than 1400 K according to these models, so in our case the hybrid isochrones are essentially equivalent to the cloudy ($f_{\text{sed}} = 2$) isochrones from SM08. We present parameters derived from the SM08 hybrid models as well as the fully cloudy and cloud free cases. We also consider the Lyon Cond models (Baraffe et al. 2003) that assume any clouds are completely below the photosphere. These, along with SM08 cloud free models, should not be appropriate for Gl 417BC because the lack of dust opacity results in spectral energy distributions highly inconsistent with L dwarfs, but they provide a useful counterpoint to the other extreme assumption made by Lyon Dusty and SM08 cloudy models about the surface boundary conditions. Finally, we include evolutionary models from Burrows et al. (1997) as they are still commonly used in the literature. These models are cloud free, use “gray” atmospheres over the temperature range considered here, and also do not benefit from updates to opacities made over the last decade.

Our method for employing the system mass and individual luminosities of a binary to derive all other properties from

evolutionary models is described in detail in our previous work (Liu et al. 2008; Dupuy et al. 2009b). Briefly, at every given age from 10 Myr to 10 Gyr we calculate the model-predicted component masses, as well as T_{eff} , $\log(g)$, radius (R), lithium abundance, and near-infrared colors, from their measured luminosities. This is done in a Monte Carlo fashion such that we use 10^3 values for a component’s L_{bol} , resulting in 10^3 mass estimates at each age. We then step through each of the 10^3 L_{bol} pairs, considering the full range of ages for that pair, sum the component masses as a function of age, and determine the age that matches the measured total mass by interpolating the curve. This is also done in a Monte Carlo fashion such that we use 10^3 values for the measured M_{tot} at this step. This results in 10^6 model-derived values for every parameter, accounting for both the errors in L_{bol} and M_{tot} and tracking the covariances with L_{bol} ratio and distance appropriately.

In Table 4, we report the median, 1σ , and 2σ confidence intervals of these parameter distributions, and we summarize some key results below.

1. *System age.* The Burrows et al. (1997) give the youngest age for the Gl 417BC system (410 ± 30 Myr) because they predict the lowest L_{bol} at this age and mass. The next youngest model-derived ages are from the SM08 hybrid and cloudy models (430 ± 40 Myr), then Lyon Dusty (490_{-50}^{+40} Myr), SM08 cloud free (540_{-40}^{+50} Myr), and Lyon Cond (570 ± 50 Myr). The SM08 hybrid/cloudy age is 2.5σ younger than the gyrochronology age we find for Gl 417A in Section 4. Only the ages derived from non-gray, cloud free models are in reasonable agreement, at $\approx 1\sigma$. This is the nearly the same level of discrepancy that we previously observed in the HD 130948BC system, which coincidentally has a very similar age and mass as Gl 417BC. We discuss the implications of this finding, as well as the differences in the luminosity evolution predicted by these models, in more detail in Section 7.
2. *Effective temperature and surface gravity.* The three sets of models we consider here give slightly different predictions for T_{eff} because of the different underlying model radii. SM08 hybrid models have the largest radii and correspondingly predict the lowest temperatures and surface gravities, with T_{eff} about 40 K cooler and $\log(g)$ about 0.03–0.04 dex lower than from Lyon Dusty models. According to the Dusty models, Gl 417B has $T_{\text{eff}} = 1750 \pm 30$ K and $\log(g) = 5.11_{-0.03}^{+0.02}$ dex (cgs), whereas the secondary Gl 417C has $T_{\text{eff}} = 1630_{-40}^{+30}$ K and $\log(g) = 5.07_{-0.03}^{+0.02}$ dex (cgs). Lyon Cond models predict values about 40 K warmer and 0.04 dex higher gravity. The various model-derived temperatures are higher than Stephens et al. (2009) found for five objects of similar spectral type (L3.5–L7) by model atmosphere fitting. They used the same model atmospheres that SM08 adopt as the boundary conditions for their evolutionary models, but Stephens et al. found that most objects were best fit by 1100–1400 K model atmospheres. Only two of their objects were fit well by 1600–1800 K model atmospheres. This suggests systematic errors in either atmospheric model spectra, evolutionary model radii, or both. A more rigorous test would be to fit the spectra of Gl 417B and Gl 417C directly, which is challenging because few spectrographs are capable of resolving such a tight binary.
3. *Mass ratio and lithium.* The model-derived mass ratios for Gl 417BC are all near unity, as expected from the modest measured flux ratios. The two most different values are from SM08 hybrid models ($q \equiv M_{\text{sec}}/M_{\text{pri}} = 0.89 \pm 0.04$)

Table 4
Evolutionary Model-derived Properties for Gl 417BC

Property	Lyon Dusty (Chabrier et al. 2000)			Lyon Cond (Baraffe et al. 2003)			Tucson (Burrows et al. 1997)		
	Median	68.3% c.l.	95.4% c.l.	Median	68.3% c.l.	95.4% c.l.	Median	68.3% c.l.	95.4% c.l.
Age (t , Gyr)	0.49	0.44, 0.53	0.41, 0.58	0.58	0.52, 0.62	0.48, 0.68	0.41	0.38, 0.44	0.34, 0.48
$\log(t/\text{yr})$	8.69	8.65, 8.72	8.62, 8.76	8.76	8.72, 8.80	8.69, 8.84	8.61	8.58, 8.65	8.54, 8.69
$M_B (M_{\text{Jup}})$	51.9	50.1, 53.7	48.3, 55.5	51.9	50.0, 53.8	48.2, 55.8	51.5	49.5, 53.2	48.0, 55.1
$M_C (M_{\text{Jup}})$	47.4	45.6, 49.1	44.1, 51.1	47.4	45.5, 49.1	43.9, 51.1	47.8	46.1, 49.5	44.5, 51.3
$q \equiv M_C/M_B$	0.91	0.88, 0.94	0.85, 0.98	0.913	0.874, 0.943	0.845, 0.976	0.929	0.901, 0.959	0.872, 0.986
$T_{\text{eff},B}$ (K)	1750	1720, 1780	1680, 1820	1790	1760, 1820	1720, 1860	1780	1740, 1810	1710, 1850
$T_{\text{eff},C}$ (K)	1630	1590, 1660	1560, 1700	1670	1630, 1700	1600, 1740	1650	1620, 1690	1580, 1730
ΔT_{eff} (K)	130	80, 170	20, 220	120	70, 170	20, 210	130	70, 170	20, 230
$\log(g_B)$ (cgs)	5.103	5.081, 5.126	5.058, 5.151	5.142	5.119, 5.164	5.096, 5.188	5.142	5.118, 5.166	5.095, 5.190
$\log(g_C)$ (cgs)	5.063	5.040, 5.085	5.019, 5.111	5.105	5.082, 5.128	5.059, 5.152	5.105	5.082, 5.128	5.058, 5.152
$R_B (R_{\text{Jup}})$	1.010	0.998, 1.022	0.983, 1.031	0.957	0.945, 0.967	0.938, 0.983	0.959	0.949, 0.969	0.939, 0.979
$R_C (R_{\text{Jup}})$	1.010	1.000, 1.021	0.987, 1.032	0.957	0.944, 0.966	0.938, 0.983	0.964	0.955, 0.974	0.945, 0.984
$(\text{Li}/\text{Li}_0)_B$	0.957	0.922, 0.978	0.742, 0.982	0.955	0.905, 0.977	0.673, 0.980	0.9935	0.991, 0.998	0.974, 1.000
$(\text{Li}/\text{Li}_0)_C$	0.975	0.967, 0.985	0.956, 0.991	0.974	0.966, 0.983	0.956, 0.991	0.9987	0.998, 1.000	0.995, 1.000
$(J - H)_B$ (mag)	1.15	1.03, 1.25	0.97, 1.39	0.066	0.046, 0.083	0.027, 0.101,, ...
$(J - H)_C$ (mag)	1.61	1.48, 1.75	1.33, 1.88	-0.001	-0.023, 0.017	-0.039, 0.042,, ...
$(H - K)_B$ (mag)	0.88	0.78, 0.95	0.73, 1.06	0.220	0.207, 0.232	0.195, 0.247,, ...
$(H - K)_C$ (mag)	1.25	1.15, 1.36	1.01, 1.46	0.204	0.198, 0.211	0.190, 0.220,, ...
$(J - K)_B$ (mag)	2.03	1.82, 2.21	1.70, 2.46	0.285	0.254, 0.313	0.226, 0.344,, ...
$(J - K)_C$ (mag)	2.86	2.63, 3.11	2.35, 3.34	0.202	0.173, 0.224	0.154, 0.257,, ...
$(K - L')_B$ (mag)	1.10	1.05, 1.14	1.02, 1.20	1.30	1.26, 1.34	1.22, 1.37,, ...
$(K - L')_C$ (mag)	1.31	1.25, 1.38	1.17, 1.43	1.42	1.38, 1.45	1.34, 1.48,, ...
Property	SM08 Hybrid			SM08 Cloudy ($f_{\text{sed}} = 2$)			SM08 Cloud Free		
	Median	68.3% c.l.	95.4% c.l.	Median	68.3% c.l.	95.4% c.l.	Median	68.3% c.l.	95.4% c.l.
Age (t , Gyr)	0.43	0.39, 0.47	0.36, 0.52	0.43	0.39, 0.47	0.36, 0.52	0.54	0.50, 0.59	0.45, 0.64
$\log(t/\text{yr})$	8.64	8.59, 8.68	8.56, 8.72	8.64	8.59, 8.68	8.56, 8.72	8.73	8.70, 8.77	8.66, 8.81
$M_B (M_{\text{Jup}})$	52.6	50.7, 54.5	48.8, 56.3	52.6	50.7, 54.4	48.8, 56.4	51.9	50.0, 53.7	48.2, 55.6
$M_C (M_{\text{Jup}})$	46.6	44.6, 48.6	42.9, 50.5	46.7	44.7, 48.6	43.0, 50.6	47.3	45.6, 49.1	43.9, 50.9
$q \equiv M_C/M_B$	0.89	0.85, 0.92	0.81, 0.97	0.89	0.85, 0.93	0.81, 0.97	0.91	0.88, 0.95	0.85, 0.98
$T_{\text{eff},B}$ (K)	1710	1670, 1740	1640, 1770	1700	1670, 1740	1640, 1770	1760	1730, 1800	1700, 1830
$T_{\text{eff},C}$ (K)	1580	1550, 1620	1520, 1650	1580	1550, 1620	1520, 1650	1640	1610, 1680	1580, 1710
ΔT_{eff} (K)	120	70, 170	20, 220	120	80, 180	30, 220	120	70, 170	30, 210
$\log(g_B)$ (cgs)	5.077	5.054, 5.102	5.030, 5.124	5.078	5.054, 5.101	5.030, 5.125	5.129	5.106, 5.151	5.082, 5.173
$\log(g_C)$ (cgs)	5.021	4.994, 5.047	4.972, 5.071	5.021	4.995, 5.046	4.971, 5.073	5.090	5.068, 5.113	5.045, 5.135
$R_B (R_{\text{Jup}})$	1.043	1.031, 1.055	1.020, 1.065	1.043	1.031, 1.055	1.019, 1.065	0.977	0.967, 0.987	0.957, 0.998
$R_C (R_{\text{Jup}})$	1.049	1.037, 1.061	1.027, 1.071	1.049	1.038, 1.061	1.026, 1.071	0.975	0.965, 0.985	0.956, 0.995
$(Y - J)_B$ (mag)	1.135	1.122, 1.151	1.111, 1.162	1.186	1.180, 1.197	1.165, 1.199	1.338	1.330, 1.346	1.319, 1.351
$(Y - J)_C$ (mag)	1.185	1.169, 1.198	1.159, 1.216	1.161	1.146, 1.179	1.131, 1.189	1.354	1.353, 1.355	1.349, 1.355
$(J - H)_B$ (mag)	0.727	0.693, 0.756	0.669, 0.796	0.699	0.661, 0.728	0.637, 0.767	0.340	0.325, 0.362	0.304, 0.375
$(J - H)_C$ (mag)	0.87	0.83, 0.91	0.77, 0.93	0.84	0.80, 0.87	0.76, 0.90	0.266	0.243, 0.291	0.219, 0.313
$(H - K)_B$ (mag)	0.648	0.613, 0.674	0.591, 0.714	0.63	0.60, 0.66	0.57, 0.69	0.079	0.054, 0.108	0.029, 0.131
$(H - K)_C$ (mag)	0.78	0.75, 0.81	0.70, 0.84	0.729	0.716, 0.748	0.686, 0.756	-0.016	-0.043, 0.013	-0.073, 0.039
$(J - K)_B$ (mag)	1.38	1.31, 1.43	1.26, 1.51	1.33	1.26, 1.39	1.21, 1.46	0.42	0.38, 0.47	0.33, 0.51
$(J - K)_C$ (mag)	1.65	1.58, 1.72	1.47, 1.77	1.56	1.52, 1.62	1.45, 1.66	0.25	0.20, 0.30	0.14, 0.35
$(K - L')_B$ (mag)	0.897	0.869, 0.914	0.863, 0.945	0.953	0.932, 0.976	0.908, 0.994	1.149	1.130, 1.165	1.113, 1.183
$(K - L')_C$ (mag)	1.000	0.972, 1.026	0.935, 1.052	1.016	1.009, 1.024	0.989, 1.029	1.216	1.195, 1.236	1.175, 1.256

Notes. Each line in the table gives the median model-derived value along with the shortest intervals containing 68.3% and 95.4% of the chain steps (i.e., 1σ and 2σ confidence limits). All photometry on the MKO system. Saumon & Marley (2008) hybrid and cloudy models give virtually identical physical parameters because the only difference is assuming $f_{\text{sed}} = 2$ for the fully cloudy models and $f_{\text{sed}} = 1$ for the cloudy portion of the hybrid models.

and the Lyon Dusty models (0.93 ± 0.03), and these are in good agreement. Combined with our total system mass, the various model-derived mass ratios and 1σ uncertainties imply primary masses of $50\text{--}56 M_{\text{Jup}}$ and secondary masses of $45\text{--}52 M_{\text{Jup}}$. Lyon Dusty, Cond, and Burrows et al. (1997) models include a prediction for the fraction of initial lithium that remains in these brown dwarfs, but even in the most extreme case (Cond, 2σ) Gl 417B is predicted to have depleted only 35% of its lithium. This is consistent with

the observation of lithium absorption in the integrated-light spectrum of Gl 417BC (Kirkpatrick et al. 2000).

4. *Near-infrared colors.* All models except Burrows et al. (1997) predict full $JHKL'$ colors for both components of Gl 417BC, though we ignore the cloud free models here because they have extremely blue colors. Our resolved photometry gives somewhat redder colors for Gl 417C compared to Gl 417B in $J-H$ and $J-K$ but slightly bluer colors for Gl 417C at $Y-J$ and $H-K$, although

these differences between the two components are only marginally significant. In comparison to model predictions, both components of Gl 417BC are redder than the SM08 models but bluer than Lyon. The level of disagreement between most of the observed and predicted colors is 0.2–0.3 mag, typical of other brown dwarfs with dynamical mass measurements (e.g., Dupuy et al. 2009b, 2010). However, the Dusty models predict colors for Gl 417C that are 0.4–1.0 mag discrepant.

7. A SUBSTELLAR LUMINOSITY PROBLEM?

Gl 417BC is only the second field brown dwarf system after HD 130948BC with a precisely measured mass, age, and luminosity. By coincidence, the two systems have very similar fundamental properties, with the exception of the projected separation of their host stars. Thus they provide two independent tests of substellar models at roughly the same age, mass, and metallicity but with objects that may have had different formation pathways and dynamical evolution. This is particularly important because our age determinations implicitly assume that the rotational evolution of the host stars is typical compared to single stars in open clusters, which are used to calibrate the gyrochronology relations. This assumption is not obvious as our first results came from HD 130948BC, where the brown dwarfs lie at a projected separation of only 47 AU from their host star. Such a separation could be consistent with HD 130948BC forming via gravitational instability in a long-lived, massive circumstellar disk (e.g., Rice et al. 2003; Stamatellos et al. 2007), and since disks are suspected to influence stellar rotation formation of a massive binary brown dwarf in the disk may have caused atypical rotational properties for HD 130948A. But if some particular mechanism was responsible for altering the rotational history of HD 130948A, it is implausible to believe that it would also be at work in the Gl 417 system. Gl 417BC is separated from its host star by 1970 AU in projection, suggesting a very different dynamical history from the HD 130948 system.

Remarkably, we find nearly the same results from these two independent tests of substellar luminosity evolution. As described in Section 6, the model-derived ages for Gl 417BC are $\approx 2\sigma$ younger than the gyro age for Gl 417A. This implies that the components of Gl 417BC are more luminous than expected given their masses and age. For comparison, we present newly derived parameters for HD 130948BC in Table 5, using the updated orbit from Dupuy & Liu (2011) and improved bolometric corrections from Liu et al. (2010). The SM08 hybrid model-derived system age for HD 130948BC is $\log(t/\text{yr}) = 8.59 \pm 0.03$ dex, and for Lyon Dusty models it is 8.65 ± 0.03 dex. These ages are 3.6σ and 2.9σ younger than the gyro age for HD 130948A, $\log(t/\text{yr}) = 8.90 \pm 0.08$ dex (Dupuy et al. 2009b).

In principle, this luminosity–age discrepancy could be caused by systematic errors either in substellar evolutionary models or in gyrochronology relations. The challenges associated with age determinations for stars are well documented (e.g., Soderblom et al. 2013, and references therein). Recent modeling of error sources in the gyrochronology age for any arbitrary field star by Epstein & Pinsonneault (2014) show that at our primary stars’ masses (1.08 – $1.11 M_{\odot}$; Takeda et al. 2007) and rotation periods (7.8–8.3 days) we may expect $\approx 20\%$ systematic errors in our derived ages, comparable to our empirically derived error bars of 0.08 dex. However, the sources of this error (differential rotation and varying initial conditions) should be essentially random, and thus it would be very unlikely for two unrelated field

stars to show the same age discrepancy. We therefore conclude that altered substellar evolution model cooling rates would provide a simpler explanation for our observed luminosity–age discrepancy, and in the following analysis we proceed under this assumption. (We note that if the cause is instead a systematic age offset present in stellar age–rotation–activity relations, this would have its own problematic implications that could range from incorrectly estimated ages for host stars of directly imaged planets to fundamental errors in the ages of the clusters used to calibrate the relations.)

To illustrate our observed luminosity–age discrepancies, we show probability distributions of the difference between model-derived system ages and gyro ages in Figure 3. We also plot the joint probability distribution that results from combining these two results. The joint distribution implicitly assumes that the components in both HD 130948BC and Gl 417BC probe similar physics because their masses are only $\approx 10\%$ – 15% different and their ages are indistinguishable, $\Delta\log(t/\text{yr}) = 0.03 \pm 0.11$ dex. The joint discrepancy in age is 4.0σ for SM08 hybrid models, 3.5σ for Lyon Dusty models, and 2.3σ for Cond. To quantify the discrepancy in terms of luminosity, we scaled up the L_{bol} values predicted by models by a constant factor to find the boost that brings the ages into exact agreement. For Lyon Dusty models, the scaling factor needed was 0.25 dex for Gl 417BC and 0.35 dex for HD 130948BC, and for SM08 hybrid models they were 0.27 dex and 0.40 dex, respectively. Lyon Cond models require the smallest boost of only 0.15 dex for Gl 417BC and 0.25 dex for HD 130948BC. The fact that the level of discrepancy varies widely between models is a reflection of the different luminosity predictions for substellar objects in different models.

7.1. The Influence of Clouds on Brown Dwarf Cooling

The inclusion of additional opacity from dust clouds has long been known to result in a lower luminosity at a given mass and age (e.g., Chabrier et al. 2000). This explains why the Lyon Dusty models are more discrepant with our unexpectedly luminous brown dwarfs than the Cond models. SM08 also note that their cloudy models are slightly lower luminosity than Lyon Dusty models. Figure 5 shows the differences in predicted luminosities as a function of age for a model object of similar mass to the binary components we consider here ($0.050 M_{\odot}$). Across a wide range of ages, and particularly from a few hundred Myr to ~ 1 Gyr, some of the most commonly used models differ in their luminosity predictions significantly. At ages of 700–800 Myr, this amounts to a ≈ 0.2 dex range in L_{bol} . Thus, mass estimates from evolutionary models are actually quite dependent on the choice of model.

A particularly interesting case shown in Figure 5 is the one set of models that attempts to account for cloud evolution as a substellar object cools. The SM08 hybrid models show a feature in L_{bol} versus age not seen in any other models: a bump in L_{bol} that accompanies the disappearance of cloud opacity from the photosphere. This is at least partly understandable because an object with no cloud opacity is more luminous, as noted above in the comparison between Lyon Cond and Dusty models. However, the SM08 hybrid models actually greatly outshine the Lyon Cond models for a few Gyr after the clouds disappear. This is not simply a consequence of differences in the energy transport budgets of the two models (Lyon models account for electron conduction that dominates $\gtrsim 2$ Gyr, while SM08 do not) because the SM08 hybrid models actually reach a similar or somewhat lower L_{bol} as Cond at 10 Gyr. Therefore, we find

Table 5
Evolutionary Model-derived Properties for HD 130948BC

Property	Lyon Dusty (Chabrier et al. 2000)			Lyon Cond (Baraffe et al. 2003)			Tucson (Burrows et al. 1997)		
	Median	68.3% c.l.	95.4% c.l.	Median	68.3% c.l.	95.4% c.l.	Median	68.3% c.l.	95.4% c.l.
Age (t , Gyr)	0.45	0.42, 0.48	0.39, 0.51	0.51	0.47, 0.54	0.44, 0.58	0.416	0.391, 0.440	0.370, 0.466
$\log(t/\text{yr})$	8.65	8.62, 8.68	8.60, 8.71	8.70	8.67, 8.73	8.65, 8.76	8.62	8.59, 8.64	8.57, 8.67
$M_B (M_{\text{Jup}})$	58.9	57.3, 60.3	55.9, 61.9	59.1	57.6, 60.7	56.0, 62.3	58.5	57.1, 59.8	55.8, 61.1
$M_C (M_{\text{Jup}})$	55.8	54.4, 57.2	53.0, 58.7	55.5	54.0, 57.1	52.5, 58.7	56.2	54.9, 57.5	53.7, 58.9
$q \equiv M_C/M_B$	0.948	0.920, 0.979	0.894, 1.013	0.94	0.91, 0.97	0.88, 1.01	0.962	0.938, 0.981	0.916, 1.003
$T_{\text{eff},B}$ (K)	1990	1960, 2030	1920, 2060	2030	1990, 2060	1960, 2090	2050	2010, 2090	1970, 2130
$T_{\text{eff},C}$ (K)	1910	1880, 1940	1840, 1970	1940	1910, 1980	1880, 2010	1960	1930, 2000	1890, 2040
ΔT_{eff} (K)	90	30, 130	-20, 180	80	30, 130	-20, 170	90	40, 140	-20, 190
$\log(g_B)$ (cgs)	5.144	5.126, 5.160	5.111, 5.180	5.171	5.155, 5.187	5.141, 5.204	5.201	5.186, 5.216	5.171, 5.230
$\log(g_C)$ (cgs)	5.123	5.107, 5.138	5.094, 5.157	5.150	5.134, 5.166	5.119, 5.184	5.184	5.169, 5.199	5.154, 5.215
$R_B (M_{\text{Jup}})$	1.017	1.007, 1.028	0.996, 1.038	0.987	0.976, 0.997	0.967, 1.009	0.955	0.948, 0.962	0.941, 0.970
$R_C (M_{\text{Jup}})$	1.016	1.005, 1.028	0.992, 1.036	0.982	0.972, 0.992	0.963, 1.004	0.955	0.948, 0.962	0.941, 0.968
$(\text{Li}/\text{Li}_0)_B$	0.46	0.32, 0.67	0.13, 0.75	0.33	0.19, 0.47	0.05, 0.61	0.902	0.873, 0.936	0.828, 0.965
$(\text{Li}/\text{Li}_0)_C$	0.72	0.62, 0.83	0.47, 0.94	0.65	0.50, 0.80	0.40, 0.97	0.950	0.931, 0.978	0.899, 0.988
$(J-H)_B$ (mag)	0.72	0.67, 0.76	0.64, 0.81	0.180	0.166, 0.196	0.148, 0.210
$(J-H)_C$ (mag)	0.82	0.77, 0.87	0.74, 0.93	0.143	0.128, 0.158	0.112, 0.173
$(H-K)_B$ (mag)	0.561	0.534, 0.587	0.508, 0.618	0.299	0.288, 0.311	0.274, 0.322
$(H-K)_C$ (mag)	0.64	0.60, 0.67	0.58, 0.71	0.275	0.262, 0.287	0.249, 0.299
$(J-K)_B$ (mag)	1.28	1.21, 1.34	1.15, 1.43	0.479	0.455, 0.509	0.425, 0.532
$(J-K)_C$ (mag)	1.46	1.38, 1.54	1.31, 1.64	0.418	0.393, 0.447	0.360, 0.468
$(K-L')_B$ (mag)	0.927	0.904, 0.951	0.879, 0.972	1.03	0.99, 1.07	0.95, 1.11
$(K-L')_C$ (mag)	0.977	0.958, 0.997	0.938, 1.016	1.12	1.08, 1.16	1.05, 1.20
Property	SM08 Hybrid			SM08 Cloudy ($f_{\text{sed}} = 2$)			SM08 Cloud Free		
	Median	68.3% c.l.	95.4% c.l.	Median	68.3% c.l.	95.4% c.l.	Median	68.3% c.l.	95.4% c.l.
Age (t , Gyr)	0.393	0.366, 0.419	0.343, 0.446	0.393	0.366, 0.418	0.343, 0.446	0.47	0.44, 0.51	0.41, 0.54
$\log(t/\text{yr})$	8.59	8.57, 8.62	8.54, 8.65	8.59	8.57, 8.62	8.54, 8.65	8.68	8.65, 8.71	8.62, 8.74
$M_B (M_{\text{Jup}})$	58.8	57.4, 60.2	56.0, 61.7	58.8	57.4, 60.2	56.0, 61.7	59.2	57.6, 60.7	56.1, 62.3
$M_C (M_{\text{Jup}})$	55.9	54.5, 57.3	53.2, 58.8	55.9	54.5, 57.3	53.2, 58.8	55.6	54.0, 57.1	52.6, 58.6
$q \equiv M_C/M_B$	0.951	0.918, 0.974	0.901, 1.007	0.951	0.922, 0.978	0.895, 1.000	0.94	0.91, 0.98	0.87, 1.00
$T_{\text{eff},B}$ (K)	1950	1910, 1990	1880, 2020	1950	1910, 1990	1880, 2020	2000	1960, 2030	1930, 2070
$T_{\text{eff},C}$ (K)	1860	1830, 1900	1800, 1930	1860	1830, 1900	1790, 1930	1920	1880, 1950	1850, 1980
ΔT_{eff} (K)	90	40, 140	-10, 180	90	40, 140	-10, 180	80	40, 140	-20, 170
$\log(g_B)$ (cgs)	5.117	5.101, 5.133	5.085, 5.148	5.117	5.101, 5.133	5.085, 5.148	5.160	5.144, 5.176	5.128, 5.192
$\log(g_C)$ (cgs)	5.095	5.079, 5.111	5.063, 5.128	5.095	5.079, 5.111	5.063, 5.127	5.138	5.122, 5.155	5.104, 5.172
$R_B (M_{\text{Jup}})$	1.054	1.045, 1.062	1.038, 1.072	1.054	1.045, 1.062	1.038, 1.072	1.006	0.996, 1.015	0.986, 1.026
$R_C (M_{\text{Jup}})$	1.055	1.046, 1.063	1.038, 1.072	1.055	1.046, 1.063	1.038, 1.072	1.000	0.990, 1.009	0.982, 1.019
$(Y-J)_B$ (mag)	1.135	1.117, 1.164	1.094, 1.167	1.122	1.119, 1.126	1.111, 1.132	1.235	1.214, 1.255	1.194, 1.274
$(Y-J)_C$ (mag)	1.138	1.122, 1.151	1.121, 1.167	1.137	1.127, 1.144	1.123, 1.157	1.280	1.266, 1.297	1.247, 1.310
$(J-H)_B$ (mag)	0.551	0.545, 0.559	0.533, 0.581	0.560	0.543, 0.574	0.533, 0.588	0.427	0.418, 0.435	0.410, 0.443
$(J-H)_C$ (mag)	0.600	0.571, 0.633	0.550, 0.649	0.593	0.579, 0.607	0.567, 0.630	0.405	0.395, 0.415	0.380, 0.422
$(H-K)_B$ (mag)	0.464	0.447, 0.479	0.430, 0.504	0.466	0.444, 0.487	0.428, 0.503	0.221	0.205, 0.236	0.188, 0.248
$(H-K)_C$ (mag)	0.522	0.495, 0.553	0.470, 0.574	0.511	0.494, 0.527	0.477, 0.555	0.185	0.165, 0.203	0.142, 0.217
$(J-K)_B$ (mag)	1.015	0.991, 1.037	0.962, 1.084	1.03	0.99, 1.06	0.96, 1.09	0.648	0.622, 0.669	0.598, 0.691
$(J-K)_C$ (mag)	1.12	1.07, 1.19	1.02, 1.22	1.104	1.073, 1.133	1.045, 1.186	0.590	0.559, 0.616	0.524, 0.639
$(K-L')_B$ (mag)	0.829	0.815, 0.861	0.792, 0.861	0.822	0.808, 0.836	0.796, 0.849	1.011	0.987, 1.035	0.962, 1.059
$(K-L')_C$ (mag)	0.8554	0.8510, 0.8580	0.8456, 0.8635	0.859	0.841, 0.873	0.829, 0.895	1.064	1.047, 1.086	1.025, 1.105

Notes. Each line in the table gives the median model-derived value along with the shortest intervals containing 68.3% and 95.4% of the chain steps (i.e., 1σ and 2σ confidence limits). All photometry on the MKO system. Saumon & Marley (2008) hybrid and cloudy models give virtually identical physical parameters because the only difference is assuming $f_{\text{sed}} = 2$ for the fully cloudy models and $f_{\text{sed}} = 1$ for the cloudy portion of the hybrid models.

that cloud evolution can have an even more profound impact on luminosity evolution than previously thought.

The SM08 hybrid models are the first to self-consistently calculate substellar evolution accounting for cloud disappearance, and they adopt a simple interpolation between cloudy and cloudless model atmospheres to do so. However, the same group has long pointed out the possibility of patchy clouds (Ackerman & Marley 2001), and they have also investigated the impact of having two types of clouds in different regions of the surface on the

colors and spectra of brown dwarfs (Marley et al. 2010). Recent observations of brown dwarf variability, particularly in the L/T transition, now provide strong evidence for such patchy clouds (e.g., Artigau et al. 2009; Radigan et al. 2012). These opacity holes are inferred to cover a significant fraction of the surface ($\sim 10\%$; Heinze et al. 2013), and this could alter model predictions of luminosity evolution as compared to SM08's smooth interpolation between cloudy and cloudless. We suggest that if cloudless regions appeared earlier, then the luminosity bump

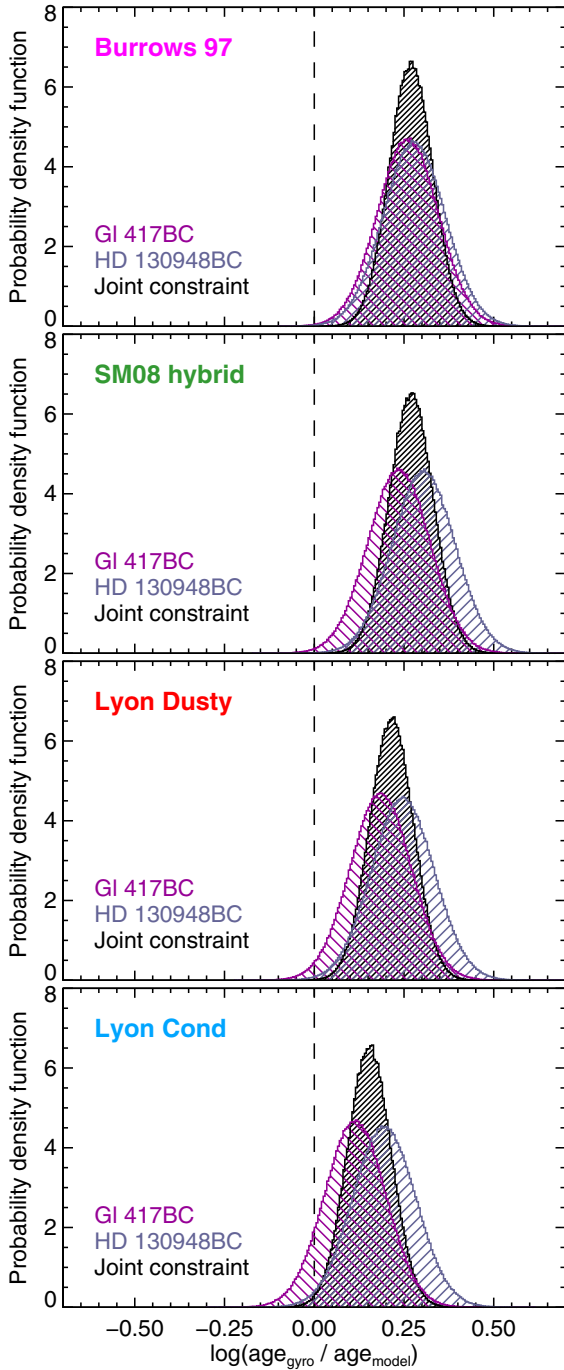


Figure 3. Probability distributions of the difference between gyrochronology ages and evolutionary model-derived ages for the brown dwarf binaries GI 417BC (violet) and HD 130948BC (blue). Multiplying these two distributions gives the joint constraint (black). For both systems, all three models predict ages that are too young based on the measured total masses and component luminosities. This indicates that model-predicted luminosities are too low for these binaries, which have similar component masses ($\approx 45\text{--}60 M_{\text{Jup}}$) and indistinguishable ages of around 800 Myr.

(A color version of this figure is available in the online journal.)

seen in SM08 hybrid models may occur earlier, i.e., at several hundred Myr instead of a few Gyr. This speculative idea could provide a solution to the over luminosity we have observed for both HD 130948BC and GI 417BC.

Finally, we note that metallicity is not likely to play a significant role in modulating L_{bol} . To illustrate this, we consider SM08 cloudless models at metallicities of -0.3 , 0.0 , and $+0.3$ dex at

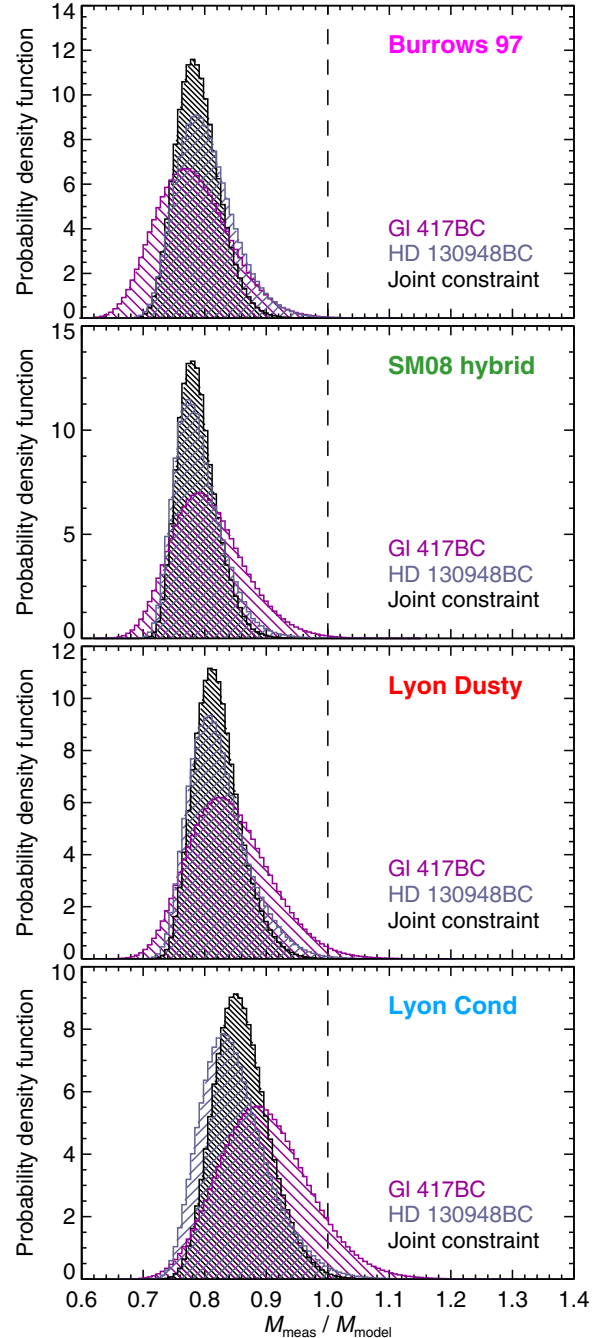


Figure 4. Probability distributions of the difference between the system masses measured dynamically and those derived from evolutionary models using component luminosities and system gyrochronology ages for the brown dwarf binaries GI 417BC (violet) and HD 130948BC (blue). Multiplying these two distributions gives the joint constraint (black). For both systems, the directly measured masses are systematically lower than predicted by all three models. This is an alternative way of viewing the same discrepancy shown in Figure 3, caused by model-predicted luminosities that are too low at this mass ($\approx 45\text{--}60 M_{\text{Jup}}$) and age (≈ 800 Myr).

(A color version of this figure is available in the online journal.)

an age of 800 Myr. The super-solar models predict L_{bol} values higher by $0.03\text{--}0.04$ dex at masses of $0.045\text{--}0.060 M_{\odot}$, whereas the sub-solar models predict $0.04\text{--}0.05$ dex lower L_{bol} for the same mass range. Thus, at the metallicities of the GI 417 and HD 130948 systems, $[\text{Fe}/\text{H}] \approx 0.0\text{--}0.1$ dex, we find from simple interpolation that the error in our model luminosities are $\lesssim 0.01$ dex by assuming solar metallicity, i.e.,

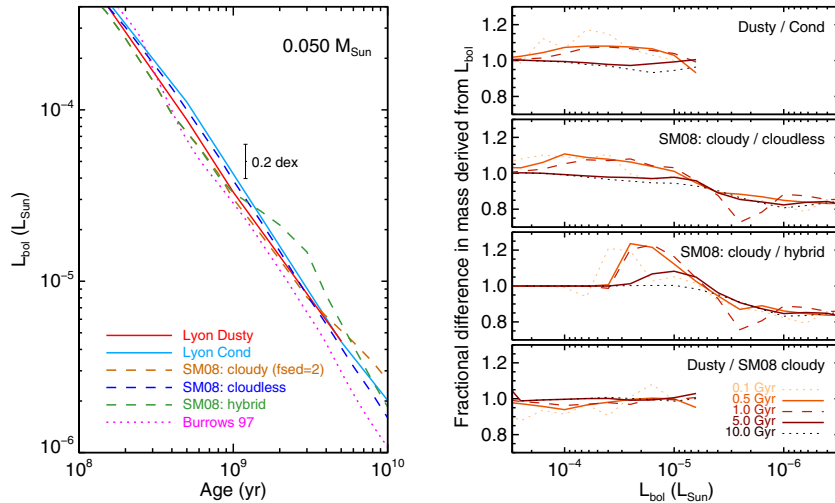


Figure 5. Left: bolometric luminosity as a function of age for a $0.050 M_{\odot}$ brown dwarf as predicted by several different evolutionary models: Dusty (Chabrier et al. 2000) and Cond (Baraffe et al. 2003) models from the Lyon group; dusty ($f_{\text{sed}} = 2$), cloudless, and hybrid models from SM08; and models from Burrows et al. (1997). The range in model predicted luminosity is typically ≈ 0.2 dex ($\approx 60\%$). Right: comparison of masses that would be derived from evolutionary models given (errorless) L_{bol} and age. Each plot shows the ratio of the masses derived from two evolutionary models, e.g., the top panel shows the Dusty model-derived masses divided by the Cond model-derived masses for the same L_{bol} and age. The impact of clouds on luminosity evolution can result in model-derived masses that differ by as much as $\pm 25\%$, as in the case of the cloudy vs. SM08 hybrid models.

(A color version of this figure is available in the online journal.)

negligible compared to our 0.03 – 0.04 dex L_{bol} measurement errors.

7.2. Implications for Model-derived Masses

According to the scaling relations presented by Burrows et al. (2001), $L_{\text{bol}} \propto M^{2.4}$ so a large systematic error in model luminosities will result in a correspondingly smaller error in masses derived from those models. To illustrate how variations in predicted luminosity evolution impact model-derived masses, Figure 4 shows the difference between our measured dynamical masses for Gl 417BC and HD 130948BC and those that we infer from evolutionary models based on the component luminosities and system ages. The Lyon Dusty models gives masses 15% – 20% (≈ 0.09 dex) higher than we measured, while the discrepancy is larger for SM08 hybrid models (20% – 25% ; ≈ 0.11 dex). The Lyon Cond models show the smallest L_{bol} discrepancy, even though they are not intended to be appropriate for these dust-bearing mid-L dwarfs, and correspondingly the masses derived from these models are only 10% – 20% (≈ 0.07 dex) higher than we measure.

To broaden our discussion beyond Gl 417BC and HD 130948BC, we show in Figure 5 the fractional differences between masses derived from the various models we consider here over a wide range of assumed ages and L_{bol} values. For example, Lyon Cond models are typically more luminous than Lyon Dusty at a given mass and age and thus masses derived from Dusty will be higher than from Cond at a given L_{bol} and age. (Note that this trend reverses at ages of 5 – 10 Gyr simply because at such old ages objects have either stabilized on the main sequence at high temperatures not significantly affected by dust or cooled to temperatures where Dusty models are not appropriate, $T_{\text{eff}} \lesssim 1000$ K.) Similar trends appear in the comparison between SM08 cloudy and cloudless models that are tracked to lower luminosities (Lyon Dusty models are not computed below $L_{\text{bol}} \approx 5 \times 10^{-6} L_{\odot}$). The largest differences in model-derived masses for the SM08 cloudy/cloudless

comparison case are $\approx 25\%$ and appear at 1 Gyr and $L_{\text{bol}} = 2 \times 10^{-6} L_{\odot}$ ($T_{\text{eff}} \approx 700$ K) because at these low temperatures SM08 cloudy models are actually more luminous than cloudless models.

As discussed above, the largest discrepancies between various model predictions of luminosity evolution all involve the SM08 hybrid models that, unlike other models, display a prominent luminosity increase as clouds disappear. Figure 5 shows that masses derived from SM08 fully cloudy models, which are nearly identical to Lyon Dusty models, are up to 25% higher than those that would be inferred from the SM08 hybrid models. The SM08 cloudy/hybrid mass discrepancy is $>10\%$ over a range in L_{bol} that corresponds to $T_{\text{eff}} \approx 1000$ – 1400 K and for ages up to ≈ 5 Gyr. Because cloud disappearance is parameterized purely by T_{eff} in the SM08 hybrid models, the same effect occurs for younger objects but at higher luminosities due to their larger radii. Therefore if cloud disappearance indeed causes such substantial changes in L_{bol} evolution, it will affect mass estimates for substellar objects of all ages, except perhaps at old ages of ~ 10 Gyr when all but the very highest mass brown dwarfs have long been without their clouds.

8. CONCLUSIONS

We have presented a dynamical mass measurement for the L4.5+L6 binary Gl 417BC based on Keck LGS AO imaging obtained over 2007–2014. Combined with reanalysis of the HST discovery images from 2001, our data now span over 13 yr of the 15.65 ± 0.09 yr orbit, allowing us to determine a precise system mass of $99 \pm 3 M_{\text{Jup}}$. The host star Gl 417A is a young solar-type star for which we derive a gyrochronology age of 750^{+150}_{-120} Myr that agrees with other (less precise) ages estimated from activity indicators, lithium, and isochrones. Gl 417BC now joins HD 130948BC as only the second system of brown dwarfs with a precisely measured mass, age, and luminosity. These two systems coincidentally have similar component masses to within 10% – 15% , indistinguishable ages,

and nearly solar composition. This makes Gl 417BC ideal for assessing the “luminosity problem” identified by our prior work on HD 130948BC, for which we found that Lyon Dusty models under-predicted the component luminosities by a factor of ≈ 2 (Dupuy et al. 2009b). Moreover, the larger projected separation (1970 AU) between Gl 417BC and its host star compared to HD 130948BC (47 AU) guards against a peculiar angular momentum history impacting stellar rotation-based age estimates.

Gl 417BC displays a nearly identical over-luminosity compared to models as we previously observed for HD 130948BC ($\Delta \log L_{\text{bol}} \approx 0.3$ dex). This new evidence strongly suggests that there is indeed a luminosity problem, at least for substellar objects with masses around 45–60 M_{Jup} at an age of ≈ 800 Myr. In search of a possible solution, we compared the luminosity predictions from currently available evolutionary models and noted that cloud disappearance can have a surprisingly large impact on luminosity evolution. While it has long been recognized that cloud opacity suppresses the luminosity of a brown dwarf at a given age and mass, recent models actually show that as clouds disappear from a dusty brown dwarf it can, for a time, outshine even cloud-free objects of the same mass and age. However, this boost to the luminosity does not occur early enough in hybrid models from Saumon & Marley (2008) to explain the over-luminosity we observe. These models adopt a smooth interpolation between cloudy and cloudless boundary conditions, but the latest observations of brown dwarf variability suggest a patchy process is likely more realistic. We therefore speculate that opacity holes may appear early enough, e.g., at mid-L spectral types like our two binaries, to initiate a luminosity boost that would bring evolutionary models into agreement with our observations.

If cloud evolution is responsible for the observed luminosity problem, evolutionary models suggest that this phase would be relatively long-lived and span ages that encompass most of the field population of brown dwarfs, from a few hundred Myr up to a few Gyr. Thus, masses derived from the commonly used dusty or cloudless evolutionary models would be over estimated by 10%–25%, even for some time after clouds disappeared from view entirely. Many of the known directly imaged gas-giant planets are L-type or L/T transition objects, so their model-derived properties would be particularly susceptible to systematic errors caused by clouds. Under our speculative assumptions, higher mass brown dwarfs ($>60 M_{\text{Jup}}$) should not be over-luminous at ≈ 800 Myr because they are still too hot to be affected by clouds, nor should brown dwarfs of similar mass to Gl 417BC and HD 130948BC that are several Gyr old, long after the L_{bol} boost has diminished.

The most direct evidence for this proposed scenario would be to measure the continuous mass–luminosity relation into the substellar regime of a young cluster, which would show clearly if there is indeed a boost in L_{bol} associated with the disappearance of clouds. Perhaps the most promising venue for a such a study is the Pleiades, given that is among the nearest young clusters and the discovery of short-period binaries suitable for dynamical mass measurements will be enabled by high-spatial resolution surveys with *JWST* and TMT AO. Young moving groups might also provide such a test, though they possess fewer members. Precise asteroseismic stellar ages of nearby stars from the TESS mission (Ricker et al. 2010) will also revolutionize the substellar model tests possible for companions to stars in the solar neighborhood. Not only will TESS data improve the accuracy of ages for stars like Gl 417 and HD 130948, they

will also enable tests at older ages where activity-age relations are poorly calibrated.

We are grateful to Josh Carter for discussions about MCMC methods; Didier Saumon and Isabelle Baraffe for providing expanded model grids and helpful discussions about substellar evolution; Joel Ayccock, Randy Campbell, Al Conrad, Heather Hershley, Jim Lyke, Jason McIlroy, Eric Nielsen, Gary Punawai, Julie Riviera, Hien Tran, Cynthia Wilburn, and the Keck Observatory staff for assistance with the Keck LGS AO observing; the anonymous referee for a constructive report; and James R. A. Davenport for distributing his IDL implementation of the cubehelix color scheme. This work was supported by a NASA Keck PI Data Award, administered by the NASA Exoplanet Science Institute. T.J.D. acknowledges support from Hubble Fellowship grant HST-HF-51271.01-A awarded by the Space Telescope Science Institute, which is operated by AURA for NASA, under contract NAS 5-26555. M.C.L. acknowledges support from NSF grant AST09-09222. Our research has employed the 2MASS data products; NASA’s Astrophysical Data System; the SIMBAD database operated at CDS, Strasbourg, France; and the SpeX Prism Spectral Libraries, maintained by Adam Burgasser at <http://www.browndwarfs.org/spexprism>. Finally, the authors wish to recognize and acknowledge the very significant cultural role and reverence that the summit of Mauna Kea has always had within the indigenous Hawaiian community. We are most fortunate to have the opportunity to conduct observations from this mountain.

Facilities: Keck:II (LGS AO, NIRC2), IRTF (SpeX)

REFERENCES

- Ackerman, A. S., & Marley, M. S. 2001, *ApJ*, 556, 872
Allard, F., Homeier, D., & Freytag, B. 2011, in ASP Conf. Ser. 448, 16th Cambridge Workshop on Cool Stars, Stellar Systems, and the Sun, ed. C. Johns-Krull, M. K. Browning, & A. A. West (San Francisco, CA: ASP), 91
Allers, K. N., & Liu, M. C. 2013, *ApJ*, 772, 79
Anderson, D. R., Collier, C. A., Hellier, C., et al. 2011, *ApJL*, 726, L19
Artigau, É., Bouchard, S., Doyon, R., & Lafrenière, D. 2009, *ApJ*, 701, 1534
Baliunas, S., Sokoloff, D., & Soon, W. 1996, *ApJL*, 457, L99
Baraffe, I., Chabrier, G., Barman, T. S., Allard, F., & Hauschildt, P. H. 2003, *A&A*, 402, 701
Barnes, S. A. 2007, *ApJ*, 669, 1167
Bouy, H., Brandner, W., Martín, E. L., et al. 2003, *AJ*, 126, 1526
Burgasser, A. J., Cruz, K. L., Cushing, M., et al. 2010, *ApJ*, 710, 1142
Burrows, A., Hubbard, W. B., Lunine, J. I., & Liebert, J. 2001, *RvMP*, 73, 719
Burrows, A., Marley, M., Hubbard, W. B., et al. 1997, *ApJ*, 491, 856
Chabrier, G., Baraffe, I., Allard, F., & Hauschildt, P. 2000, *ApJ*, 542, 464
Crepp, J. R., Johnson, J. A., Fischer, D. A., et al. 2012, *ApJ*, 751, 97
Cutri, R. M., et al. 2003, 2MASS All Sky Catalog of Point Sources (The IRSA 2MASS All-Sky Point Source Catalog, NASA/IPAC Infrared Science Archive. <http://irsa.ipac.caltech.edu/applications/Gator/>)
de Bruijne, J. H. J., & Eilers, A.-C. 2012, *A&A*, 546, A61
Deleuil, M., Deeg, H. J., Alonso, R., et al. 2008, *A&A*, 491, 889
Diolaiti, E., Bendinelli, O., Bonaccini, D., et al. 2000, *A&AS*, 147, 335
Duncan, D. K. 1981, *ApJ*, 248, 651
Dupuy, T. J., & Liu, M. C. 2011, *ApJ*, 733, 122
Dupuy, T. J., & Liu, M. C. 2012, *ApJS*, 201, 19
Dupuy, T. J., Liu, M. C., & Bowler, B. P. 2009a, *ApJ*, 706, 328
Dupuy, T. J., Liu, M. C., Bowler, B. P., et al. 2010, *ApJ*, 721, 1725
Dupuy, T. J., Liu, M. C., & Ireland, M. J. 2009b, *ApJ*, 692, 729
Dupuy, T. J., Liu, M. C., & Ireland, M. J. 2009c, *ApJ*, 699, 168
Epstein, C. R., & Pinsonneault, M. H. 2014, *ApJ*, 780, 159
Ford, E. B. 2005, *AJ*, 129, 1706
Ford, E. B. 2006, *ApJ*, 642, 505
Fortney, J. J., Ikoma, M., Nettelmann, N., Guillot, T., & Marley, M. S. 2011, *ApJ*, 729, 32

- Gagné, J., Lafrenière, D., Doyon, R., Malo, L., & Artigau, É. 2014, *ApJ*, **783**, 121
- Gaidos, E. J., Henry, G. W., & Henry, S. M. 2000, *AJ*, **120**, 1006
- Gray, R. O., Corbally, C. J., Garrison, R. F., McFadden, M. T., & Robinson, P. E. 2003, *AJ*, **126**, 2048
- Heinze, A. N., Metchev, S., Apai, D., et al. 2013, *ApJ*, **767**, 173
- Hempelmann, A., Schmitt, J. H. M. M., Schultz, M., Ruediger, G., & Stepien, K. 1995, *A&A*, **294**, 515
- Ireland, M. J., Kraus, A., Martinache, F., Lloyd, J. P., & Tuthill, P. G. 2008, *ApJ*, **678**, 463
- Johnson, J. A., Apps, K., Gazak, J. Z., et al. 2011, *ApJ*, **730**, 79
- Kirkpatrick, J. D., Cruz, K. L., Barman, T. S., et al. 2008, *ApJ*, **689**, 1295
- Kirkpatrick, J. D., Dahn, C. C., Monet, D. G., et al. 2001, *AJ*, **121**, 3235
- Kirkpatrick, J. D., Reid, I. N., Liebert, J., et al. 2000, *AJ*, **120**, 447
- Konopacky, Q. M., Ghez, A. M., Barman, T. S., et al. 2010, *ApJ*, **711**, 1087
- Krist, J. 1995, in ASP Conf. Ser. 77, *Astronomical Data Analysis Software and Systems IV*, ed. R. A. Shaw, H. E. Payne, & J. J. E. Hayes (San Francisco, CA: ASP), 349
- Lane, B. F., Zapatero Osorio, M. R., Britton, M. C., Martín, E. L., & Kulkarni, S. R. 2001, *ApJ*, **560**, 390
- Leconte, J., & Chabrier, G. 2013, *NatGe*, **6**, 347
- Liu, M. C., Dupuy, T. J., Bowler, B. P., Leggett, S. K., & Best, W. M. J. 2012, *ApJ*, **758**, 57
- Liu, M. C., Dupuy, T. J., & Ireland, M. J. 2008, *ApJ*, **689**, 436
- Liu, M. C., Dupuy, T. J., & Leggett, S. K. 2010, *ApJ*, **722**, 311
- Malo, L., Doyon, R., Lafrenière, D., et al. 2013, *ApJ*, **762**, 88
- Mamajek, E. E., & Hillenbrand, L. A. 2008, *ApJ*, **687**, 1264
- Markwardt, C. B. 2009, in ASP Conf. Ser. 411, ed. D. A. Bohlender, D. Durand, & P. Dowler (San Francisco, CA: ASP), 251
- Marley, M. S., Saumon, D., & Goldblatt, C. 2010, *ApJL*, **723**, L117
- Mermilliod, J.-C., & Mermilliod, M. 1994, *Catalogue of Mean UBV Data on Stars* (New York: Springer)
- Monet, D. G., Levine, S. E., Canzian, B., et al. 2003, *AJ*, **125**, 984
- Mullan, D. J., & MacDonald, J. 2010, *ApJ*, **713**, 1249
- Radigan, J., Jayawardhana, R., Lafrenière, D., et al. 2012, *ApJ*, **750**, 105
- Rice, W. K. M., Armitage, P. J., Bonnell, I. A., et al. 2003, *MNRAS*, **346**, L36
- Ricker, G. R., Latham, D. W., Vanderspek, R. K., et al. 2010, *BAAS*, **42**, 459
- Saumon, D., & Marley, M. S. 2008, *ApJ*, **689**, 1327
- Simons, D. A., & Tokunaga, A. 2002, *PASP*, **114**, 169
- Siverd, R. J., Beatty, T. G., Pepper, J., et al. 2012, *ApJ*, **761**, 123
- Skumanich, A. 1972, *ApJ*, **171**, 565
- Soderblom, D. R. 1985, *AJ*, **90**, 2103
- Soderblom, D. R., Fedele, S. B., Jones, B. F., Stauffer, J. R., & Prosser, C. F. 1993a, *AJ*, **106**, 1080
- Soderblom, D. R., Hillenbrand, L. A., Jeffries, R. D., Mamajek, E. E., & Naylor, T. 2013, arXiv:1311.7024
- Soderblom, D. R., Pilachowski, C. A., Fedele, S. B., & Jones, B. F. 1993b, *AJ*, **105**, 2299
- Stamatellos, D., Hubber, D. A., & Whitworth, A. P. 2007, *MNRAS*, **382**, L30
- Stassun, K. G., Mathieu, R. D., & Valenti, J. A. 2006, *Natur*, **440**, 311
- Stephens, D. C., Leggett, S. K., Cushing, M. C., et al. 2009, *ApJ*, **702**, 154
- Stevenson, D. J. 1980, *Sci*, **208**, 746
- Takeda, G., Ford, E. B., Sills, A., et al. 2007, *ApJS*, **168**, 297
- Tokunaga, A. T., Simons, D. A., & Vacca, W. D. 2002, *PASP*, **114**, 180
- Valenti, J. A., & Fischer, D. A. 2005, *ApJS*, **159**, 141
- van Dam, M. A., Bouchez, A. H., Le Mignant, D., et al. 2006, *PASP*, **118**, 310
- van Leeuwen, F. 2007, *A&A*, **474**, 653
- Wizinowich, P. L., Le Mignant, D., Bouchez, A. H., et al. 2006, *PASP*, **118**, 297
- Yelda, S., Lu, J. R., Ghez, A. M., et al. 2010, *ApJ*, **725**, 331